Characterization of Murine Astrocyte Cultures in 3D Hydrogel Matrices

Maria Beatriz Sereno Fernandes

beatriz.sereno.fernandes@tecnico.ulisboa.pt

Instituto Superior Técnico, Lisboa, Portugal
March 2025

ABSTRACT

Three-dimensional (3D) cultures in hydrogel matrices provide a promising platform for studying astrocyte biology and advancing cell therapy applications as they can partially mimic the 3D environment found in the brain tissue. Nevertheless, further refinement and characterization are necessary to advance hydrogel platforms for astrocyte cultures. This study combines experimental and computational approaches to characterize postnatal murine astrocyte cultures in 3D alginate- and fibrin-based hydrogels. Experimentally, various hydrogel platforms, such as pure alginate, pure fibrin and fibrin-alginate composites, were evaluated for cell viability, morphology and astrocytic marker expression. Fibrin-alginate hydrogels crosslinked with 100 mM $CaCl_2$ were found to hold promising cell profiles, presenting a mean percentage of ramified cells exceeding 70%, $SOX9^+$ cell percentage of 87% and $GFAP^+/SOX9^+$ cell percentage of 89%. Computationally, a 3D nuclei segmentation deep learning model was implemented using nnU-Net. Robust performance across diverse hydrogel-based datasets with error rates below 5% was achieved. Limited functionality was found for nuclei segmentation on tissue sample datasets with high cell density. To streamline data analysis and processing, a graphical user interface was developed enabling automatic nuclei detection and multi-label cell classification of z-stack microscopy images. This tool reduces manual effort on biological image analysis and enables the generation of classification datasets. The developed computational tools are specifically designed for astrocyte culturing in hydrogel matrices. Nevertheless, this project underscores the value of integrating computational tools for automated neural tissue profiling, contributing to downstream applications in neuroscience, regenerative medicine, and tissue engineering.

Keywords: 3D astrocyte cultures, nuclei segmentation, biological image analysis, fibrin-alginate hydrogels, deep learning

1. Introduction

Neuroscience has witnessed groundbreaking advancements in the past few decades, particularly in understanding brain plasticity and cellular dynamics within the central nervous system (CNS). One such revelation is the recognition of neurogenesis – the generation of new neurons – in the adult brain, which challenged the long-standing notion that neuronal populations are static post-development [1]. This discovery has profound implications for addressing neurodegenerative diseases, cognitive decline, and brain injuries. Neurogenesis occurs in specific brain niches, such as the subventricular zone and the hippocampal dentate gyrus [2, 3], where neural stem cells (NSCs) contribute to the replenishment of neuronal populations. Despite the progress, the underlying mechanisms of neurogenesis remain incompletely understood, driving ongoing research in this domain [4].

Historically, neurons have been the focal point of CNS studies due to their role as the primary signaling units of the nervous system [5]. However, glial cells, historically regarded as mere supportive elements, have emerged as key contributors to brain function and pathology [6]. Among glial cells, astrocytes have garnered significant attention for their diverse roles in maintaining brain homeostasis, supporting synaptic activity, and responding to trauma and neurodegeneration [7]. Astrocytes not only contribute to the CNS's structural and metabolic stability but also demonstrate remarkable plasticity. Their capacity for direct reprogramming into neurons, both in vitro and in vivo, positions them as promising candidates for regenerative therapies targeting neuronal loss in conditions such as Alzheimer's disease (AD), Parkinson's disease (PD), and traumatic brain injuries [8, 9]. However, the therapeutic potential of astrocytes remains constrained by the heterogeneity and complexity of their cellular behavior, necessitating deeper exploration and characterization [10].

A critical challenge in brain research is replicating the intricate microenvironment of the CNS in vitro [11]. Traditional two-dimensional (2D) monolayer cultures, although extensively used in research, fail to mimic the 3D architecture and extracellular matrix (ECM) interactions characteristic of brain tissues. This limitation often leads to alterations in cell morphology, behavior, and gene expression, compromising the translational relevance of experimental findings [12]. To address these limitations, 3D culture systems, in particular hydrogel-based matrices, have emerged as a powerful alternative [13]. Hydrogel-based matrices, provide a more physiologically relevant environment for studying cellular dynamics. Hydrogels, composed of crosslinked polymer networks, mimic the ECM by offering a supportive and tunable microenvironment that facilitates nutrient exchange, cell adhesion, and long-term viability [14]. Their versatility allows precise control over mechanical and biochemical properties, making them ideal for brain tissue modeling [15].

Among hydrogel materials, alginate and fibrin stand out due to their unique tunability and biomimetic properties, well-suited for brain tissue modelling [16, 17]. Alginate, a natural polysaccharide derived from brown algae, offers excellent biocompatibility, tunable stiffness, and stability,

though it lacks intrinsic cell adhesion motifs [18]. Fibrin, on the other hand, is a naturally bioactive material that promotes cell attachment and differentiation but is prone to enzymatic degradation [19]. Hybrid hydrogels combining alginate and fibrin leverage the strengths of both materials, creating scaffolds that balance structural integrity with bioactivity [20]. Despite these advancements, the optimization of hydrogel formulations for astrocyte cultures remains an area of active investigation, with a focus on parameters such as crosslinking density, stiffness, and nutrient diffusion [17].

To complement these experimental advancements, computational tools have revolutionized the analysis of biological systems [21]. Machine learning (ML) and deep learning (DL) approaches have proven particularly effective in automating complex tasks such as cell detection, segmentation, and classification in biological images [22]. These tools promise to address the challenges posed by the heterogeneity and complexity of astrocyte populations, enabling high-throughput analysis with reduced manual effort [23].

Notably, convolutional neural networks (CNN)-based models excel in numerous computer vision tasks. Key frameworks for 2D instance segmentation tasks include Mask R-CNN [24], Stardist 2D [25], and Cellpose [26]. In particular, these tools offer platforms for nuclei prediction in fluorescent images and allow fine-tuning their models to specific datasets. On the other hand, nnU-Net [27], Stardist 3D [28] and Cellstitch [29] are alternatives for segmentation of 3D volumes. Among these, nnU-Net is the only having to be trained from scratch, however its self-configuring deep learning framework that automates model optimization based on input data characteristics is an appealing feature driving researchers to study its applicability in biomedical image analysis. It excels in both 2D and 3D semantic segmentation tasks, achieving state-of-the-art (SOTA) performance without requiring extensive manual tuning. Cellstitch employs a 2D approach leveraging the Cellpose 2D algorithm to segment individual cell instances in an initial step, and subsequently, a complementary algorithm reconstructs 3D segmentations from z-stack images.

This work aims to bridge experimental and computational methodologies to characterize murine astrocyte cultures in hydrogel matrices. Experimentally, it investigates the effects of various hydrogel platforms, including pure alginate, pure fibrin, and alginate-fibrin hydrogels, on astrocyte viability, morphology, and astrocytic marker expression – GFAP and SOX9. Computationally, it develops automated pipelines for 2D and 3D nuclei segmentation, leveraging state-of-the-art DL models. Additionally, a graphical user interface (GUI) was implemented to facilitate user-friendly annotation and data analysis, streamlining the study of 3D cell cultures.

The integration of these approaches seeks to advance our understanding of astrocyte behavior in 3D environments, optimize hydrogel-based culture systems, and contribute to the broader goal of developing effective therapeutic strategies for CNS repair and regeneration.

2. Experimental Methods

2.1. Primary Cultures of Mouse Cortical Astrocytes

Cortical gray matter (GM) astrocytes were isolated and cultured from postnatal day 5-7 (p5-7) wild type (WT) and transgenic Actin::GFP mice, following a reference protocol [30] with minor modifications. Whole brains were extracted from decapitated mice and transferred to a culture dish containing 10 mL of ice-cold dissection medium (1X HBSS with 10 mM HEPES). Brains were coronally sectioned at the optic chiasm, discarding the anterior portion and midbrain. Each brain was hemisected, and the hypothalamus, striatum, and cortical white matter were excised, followed by meninges removal. Cortical GM was mechanically dissociated in 3 mL of dissection medium and centrifuged at 350 rpm for 5 minutes. Cell pellet was resuspended in 5 mL of astrocyte medium (DMEM/F12 (1:1), 10% fetal bovine serum, 100 U/ml penicillin-strepomycin, supplemented with 1X B27, 0.45% glucose and 1X GlutaMAX) and plated in a T25 flask. Cells were cultured for 7 days under standard incubation conditions (37 °C, 5% CO_2). For passaging, cells were incubated at standard incubation conditions for 8 minutes with 1 mL of 0.05% trypsin. Cell solution was centrifuged at 350 rpm for 5 minutes with 1:4 astrocyte medium. Cell pellet was resuspended in astrocyte medium and filtered through a FACS filter to avoid culture of cell aggregates.

2.2. Monolayer Cell Cultures

Monolayer cell cultures were prepared in poly-D-lysine (PDL)-coated glass coverslips or PDL-coated glass-bottom 24-well plates (IBIDI) with a final concentration of 25.000 cells per well. The cell count was determined using the trypan blue exclusion method, with a 1:1 ratio of cell suspension to trypan blue. The cells were counted in Neubauer chambers under transmitted light microscopy. Cultures were supplied with 1 mL of astrocyte medium and maintained in standard incubation conditions for 7 days.

2.3. Cell Embedding in Sodium Alginate Hydrogels

Alginate hydrogels, medium viscosity guluronate (MVG) and very low viscosity guluronate (VLVG), were prepared at a concentration of 0.5% (w/v) in 1X PBS from a 2% (w/v) stock solution (Novatach™, guluronic acid $\geqslant$ 60%). Alginate solutions were mixed with cortical GM cells to achieve a final concentration of 1.000.000 cells/mL. Cell-containing alginate precursor solution was added to glass-bottom mini-wells in a 24-well plate in volumes of 15 μL. Hydrogels were covered with a dialysis membrane (Spectrum Laboratories) and crosslinked with calcium chloride solution, 100 mM for MVG and 175 mM for VLVG, for 10 minutes immediately after casting at 22 °C, room temperature. Mini-wells were flipped upside down 1 minute after the addition of calcium chloride solution, to avoid cell sedimentation. Cell-containing hydrogels were supplemented with astrocyte medium and stored at standard incubation conditions.

2.4. Cell Embedding in FibrinVLVG and Fibrin Hydrogels

The preparation of FibrinVLVG and fibrin hydrogels was consistent across all conditions, differing only in the composition of the thrombin solution and fibrinogen solution, as described on Table 1. The thrombin solution was added to the cell pellet, followed by the fibrinogen solution, in a 1:1 ratio. The cell-containing hydrogel solutions were prepared with a final cell concentration of 1.000.000 cells/mL. For hydrogel casting in mini-wells, 15 μL of the cell-containing hydrogel precursor solution was pipetted into glass-bottom mini-wells in a 24-well plate. Whereas for hydrogel casting into glass-bottom 24-well plates, 50 μL drops of the cell-containing hydrogel precursor solution were cast the middle of each well. Hydrogels gelled at room temperature for 10 minutes. FibrinVLVG hydrogels were crosslinked 1 mL of calcium chloride for 10 minutes. Hydrogels were supplemented with astrocyte medium and further incubated under standard conditions.

2.5. Immunocytochemistry

Cells were fixed at 22 ℃, room temperature, for 15 minutes with 1 mL of 4% PFA in 1X HBSS. Cells were washed thrice for 15 minutes with 1 mL of 1X HBSS, before incubation with the blocking buffer (1X PBS, 2% BSA, 0.5% Triton X-100) to permeabilize the cells and reduce nonspecific antibody binding for 1 hour at room temperature. Cells were incubated with 0.5 mL of the primary antibodies solution (1X HBSS, chicken anti-GFAP 1:1500, rabbit anti-SOX9 1:1000) for 24 hours at -4 ℃. Cells were washed thrice for 15 minutes with 1X HBSS and incubated for 2 hours at room temperature, or overnight at -4 ℃, with 0.5 mL of the secondary antibodies solution (1X HBSS, AF 647 goat anti-chicken IgY H&L 1:1000, AF594 donkey anti-rabbit IgY H&L 1:1000). Cells were washed thrice for 15 minutes with 1X HBSS. DAPI was added to the washing solution on the second washing period, in a concentration 1:1000.

2.6. LIVE/DEAD Viability Assay

Cells were washed once with 1 mL 1X PBS and stored under standard incubation conditions with 0.5 mL of a solution containing 1X PI, 10 μM Calcein-AM and Hoechst 33342 1:1000 in 1X HBSS for 45 minutes. Cells were washed with 1X PBS and fed with astrocyte medium for immediate live imaging at the confocal microscope. Live cells were identified by green fluorescence from Calcein[+], while dead cells were marked by PI staining.

2.7. Confocal Imaging of 3D Astrocyte Cultures

Mini-well cultures were imaged at the LSM710 laser-scanning confocal (Carl Zeiss). Digital images were acquired using the ZEN software (Carl Zeiss) at 10X or 20X. Images were acquired with immersion on 1X HBSS. Glass-bottom well-plates were imaged at a STELLARIS 8 FALCON on DMi8 (Leica Microsystems) confocal microscope. Digital images were acquired using the LAS-X software (Leica Microsystems), at 10X or 20X dry. Frame size was fixed at a resolution of 1024×1024 pixels, with a pixel dwell time of ranging between 2 and 3 μs. Zoom was varied between x0.75 and x1. Step size in the vertical direction was fixed at 2 μm.

2.8. Cell Morphology and Markers Expression Quantification

Astrocytic cells were identified by the expression of the nuclear marker SOX9. Astrocytes' morphology was characterized by visual inspection of GFP and GFAP channels and distinguished into three subtypes: round – cells with no visible branching; branched – cells with small branches and/or only 1 or 2 large branches, or branches that expand concentrically rather than radially; hBranched – cells with at least 3 large branches expanding radially. Additionally, cell clusters were characterized by cell aggregates containing at least three DAPI[+] nuclei and not exhibiting branching structures. SOX9^{+} nuclei aggregates with at least three nuclei which exhibit astrocyte-like branched morphologies fall into the categories of branched or hBranched, according to the previous description. Cell cultures were quantified regarding the percentage of astrocytes (SOX9^{+}/DAPI[+]), percentage of GFAP^{+} expressing cells (GFAP[+]/DAPI[+]) and percentage of reactive astrocytes (GFAP[+]/SOX9^{+}).

3. Computational Methods

3.1. Data

The dataset used for the 2D nuclei segmentation task, encompassed 21 bidimensional images with dimensions 1024×1024 pixels over a field of view (FOV) of 591.05 μm^2. The images were acquired from 7 day ADLH1L1 p5-7 mice astrocyte cell cultures embedded in 3D volume hydrogels. The cultures were imaged in a confocal microscope as z-stacks. Subsequently, the maximum intensity projections of the DAPI channel were obtained and preprocessed with Fiji to normalize, optimize the contrast and minimize the noise.

The dataset used for 3D nuclei segmentation task, encompassed 16 z-stack multichannel images obtained with confocal microscopy. The images were from 7 day ADLH1L1 p5-7 mice astrocyte cell cultures and contained the DAPI and GFAP marker channels. The images size encompassed dimensions of 512×512×101 pixels correponding to a FOV of 200.05 μm^2×200 μm. Further, the images were preprocessed manually using Fiji and included strategies to reduce background noise and optimize contrast levels. Data augmentation was also applied at a random rate of 0.3 and included 90° rotations, horizontal and vertical flips, and zoom operations ranging from x0.5 to x2. Different datasets were created from the initial one encompassing these transformations. Its description is highlighted on Table 2.

Further, four additional z-stack image datasets obtained with confocal microscopy of the DAPI channel were used to validate the 3D nuclei segmentation model. These were derived from both hydrogel cultures and murine tissue samples:

Table 1: Composition of thrombin and fibrinogen solutions for Fibrin and FibrinVLVG hydrogels casting.

	Fibrinogen Solution	Thrombin Solution
Fibrin	1X PBS 6 mg/ml fibrinogen 0.16 mg/mL aprotinin	astrocyte medium 4 U/mL thrombin
5 mM Ca^{2+} FibrinVLVG	1X PBS 6 mg/ml fibrinogen 0.16 mg/mL aprotinin 1% (w/v) VLVG	astrocyte medium 4 U/mL thrombin 10 mM CaCl$_2$
50 mM, 100 mM and 175 mM Ca^{2+} FibrinVLVG	1X PBS 6 mg/ml fibrinogen 0.16 mg/mL aprotinin 1% (w/v) VLVG	astrocyte medium 4 U/mL thrombin 10 mM CaCl$_2$

1. **Murine-derived astrocyte cultures in 3D hydrogel**: 7 day cultures of p5-7 Actin::GFP mice astrocytes in 3D hydrogels (N = 13). Single-cell distribution with FOV of 387.88 μm^2.

2. **hiPSC-derived astrocyte cultures in 3D hydrogel**: 7 day cultures of p30-35 human induced pluripotent stem cells (hiPSC) differentiated into astrocyte and seeded in 3D hydrogels (N = 9). Cultures with single-cell distribution, with FOV of 591.05 μm^2.

3. **Murine embryo tissue**: tissue of embryo WT mice (N = 9). Images of packed neural cells in a FOV of 228.12 μm^2.

4. **Murine cortex tissue**: tissue of mice cortex (N = 9). Images of packed neural cells in a FOV spanning from 122.17 μm^2 to 400.29 μm^2.

3.2. 2D Cell Nuclei Segmentation

Mask R-CNN model pretrained on the nuclear detection challenge 2018 (DSB2018) dataset was fine tuned to our own dataset. Two k-fold cross-validation experiments were conducted, using k = 3 and k = 7. Additionally, the impact of data augmentation strategies on the model's performance was also investigated. There were used strategies such as feature scaling, standard normalization, horizontal and vertical flips, Poisson noise addition, rotations, intensity amplification, contrast and brightness adjustments, gamma correction, thresholding, and Gaussian blurring. These augmentations were applied randomly, modifying training and validation images at predefined rates. The fine-tunned models performance was compared to pretrained models from ImageNet (*imagenet*) and DSB2018 (*bsd2018*) datasets. Additionally, the best performing fine-tuned model was compared to Stardist 2D and Cellpose, by testing the same dataset.

3.3. 3D Cell Nuclei Segmentation

Dataset 1 (see Table 2) was used to train nnU-Net, and compare its performance to SOTA models from Stardist 3D and Cellstitch without fine-tuning. Further, nnU-Net was trained from scratch with each of the remaining datasets presented on Table 2 under a 5-fold cross-validation method. The models' performances were statistically compared. The best performing model was further validated on unseen datasets both from hydrogel astrocyte cultures and mice tissue (see Subsection 3.1).

3.4. Evaluation Metrics

Traditional classification and object segmentation metrics were used to assess the different models' performance. The intersection over union (IoU),

$$IoU_i = \frac{1}{L} \cdot \sum_{j=1}^{L} I(z_i^{(j)} = \hat{z}_i^{(j)}), \quad (1)$$

with $i = 1, ..., N$ and $j = 1, ..., L$, is the fraction of accurate target-variable classifications over the total number of target-variables. Furthermore, the mean IoU provides a global metric for the model's performance. The mAP is calculated for each class c_k with reference to specific IoU threshold values, τ,

$$mAP_\tau^k = \frac{TP}{TP + FP + FN}, \quad (2)$$

as well as the precision,

$$precision_\tau^k = \frac{TP}{TP + FP}, \quad (3)$$

the recall,

$$recall_\tau^k = \frac{TP}{TP + FN}, \quad (4)$$

and the F1-score,

$$F1\text{-}score_\tau^k = 2 \cdot \frac{precision_\tau^k \cdot recall_\tau^k}{precision_\tau^k + recall_\tau^k}, \quad (5)$$

Further, the predictions ratio (PR),

$$PR = \frac{TP + FP}{TP + FP + FN}, \quad (6)$$

was calculated. The numerator corresponds to the number of model predictions and the denominator to the number of ground truth predictions. PR is independent of the IoU value and estimates how many nuclei the model predicts in comparison to the ground truth annotation. The number of ground truth predictions that are aggregated as a single nuclei prediction was also computed as the aggregation ratio (AR),

$$AR = \frac{aggregated\ predictions}{TP + FP + FN}, \quad (7)$$

where the numerator computes the number of ground truth instances that were aggregated in a unique prediction by the model.

Table 2: Depiction of the datasets generated for nnU-Net model optimization.

Features	dataset 1	dataset 2	dataset 3	dataset 4	dataset 5
Images	preprocessed	raw	raw	raw + augmented	raw + augmented
Size	16	16	16	120	150
Selected Channels	DAPI + GFAP	DAPI + GFAP	DAPI	DAPI	DAPI
Augmentation	–	–	–	rotations vertical and horizontal flips	rotations vertical and horizontal flips, zoom
Digital Size (512,512,101,Z)	Z = 2	Z = 2	Z = 1	Z = 1	Z = 1
Training FOV Range (μm^2)	200.63	200.63	200.63	200.63	100.31 − 802.50
nnU-Net Model	*model 1*	*model 2*	*model 3*	*model 4*	*model 5*

4. Computational Results and Discussion

Computationally, deep learning models were trained for nuclei segmentation in both 2D fluorescent microscopy images (Subsections 4.1 and 4.2) and fluorescent microscopy z-stacks (Subsections 4.3 – 4.5). Their performance was then evaluated against SOTA models and assessed on unseen datasets. Furthermore, key advancements in the GUI for z-stack image annotation are detailed in Subsection 4.6.

4.1. Mask R-CNN performs effectively even when fine-tuned on a limited-size dataset

The Mask R-CNN *dsb2018* model – pretrained on a nuclei segmentation dataset –, achieved significantly increased performance than the Mask R-CNN *imagenet* model – targeted to broader image segmentation applications. Nevertheless, *dsb2018* model still achieved underperforming results with recall of 0.47 and a mAP of 0.41 given a $\tau = 0.2$, and a PR of 0.52, which remains very inacurate for practical uses.

The fine-tuned models of Mask R-CNN demonstrated superior performance, when considering the testing on the same dataset. Namely, the best performing fine-tuned model was trained without employing data augmentation strategies and with the 3-fold cross-validation. Thus 7 different models were trained with 18 images from the 21-image dataset and validated with the remaining ones. It achieved recall of 0.90 and mAP of 0.85 given $\tau = 0.2$, and a PR of 0.88.

These high performing results, underscore the solid performance of Mask R-CNN even when fine-tuned to a limited size dataset. Nevertheless, the results were not validated on unseen datasets from z-stack hydrogel images from astrocytes or other types of cells. Therefore, it remains incompletely understood if the model performance can be generalized to segment nuclei of other hydrogel cell cultures.

4.2. Trained from scratch Mask R-CNN model outperforms SOTA Stardist 2D and Cellpose

The best performing Mask R-CNN model was further compared to SOTA models from Stardist 2D and Cellpose. Stardist 2D, pretrained with nuclei segmentation data from the DSB2018 dataset, showed very competitive results obtained with the Mask R-CNN. There was obtained a PR of 1.09, which indicates Stardist 2D may overestimate the number of nuclei predictions. The IoU ratio was also superior than that of the Mask R-CNN model, with a performance of 0.65 compared to 0.63. Nevertheless, Mask R-CNN still overperforms regarding the recall, precision and mAP values given a $\tau = 0.2$. Mask R-CNN achieved values of 0.90, 0.94, and 0.85 for recall, precision and mAP values, respectively, whereas Stardist 2D achieved performances of 0.88, 0.86 and 0.77 for the same metrics respectively.

While the underperformance of Stardist compared to Mask R-CNN was not substantial, the underperformance of Cellpose was significant. Cellpose exhibited a strong tendency to substantially overestimate the number of nuclei observed in the images with a PR value of 4.68. Furthermore, the precision and mAP values given a $\tau = 0.2$ were of 0.27 and 0.25, respectively. Additionally, Cellpose exhibited significantly longer estimation times, taking up to 60 times longer than alternative models to produce predictions. These results discourage further investigation of Cellpose for the given purposes.

Contrastingly, the results suggested that Stardist 2D is a strong alternative to Mask R-CNN. Fine-tuning Stardist model to the dataset might increase its performance even further. Additionally, amplifying the dataset size with images from hydrogel cultures might increase the models performance in this setting. Nevertheless, the careful annotation of complementary images for this purpose presents a considerable bottleneck to the investigation.

Further assessments into 2D nuclei segmentation were not pursued. Two-dimensional image segmentation is inherently limited by its inability to account for the three-dimensionality of the cell cultures. Consequently, exploring 3D nuclei segmentation is more pertinent to this work, as it provides a more accurate representation of the culture's characteristics.

4.3. nnU-Net model outperforms SOTA models from Stardist 3D and Cellstitch

The nnU-Net model was tested against Stardist 3D and Cellstitch. This experiment aimed to assess if training nnU-Net from scratch could yield better results than SOTA models pretrained on nuclei segmentation datasets. Across all assessed metrics, nnU-Net consistently outperformed its counterparts (Figure 1). Not only are its mean values closer to the optimal, but the 95% confidence intervals are narrower.
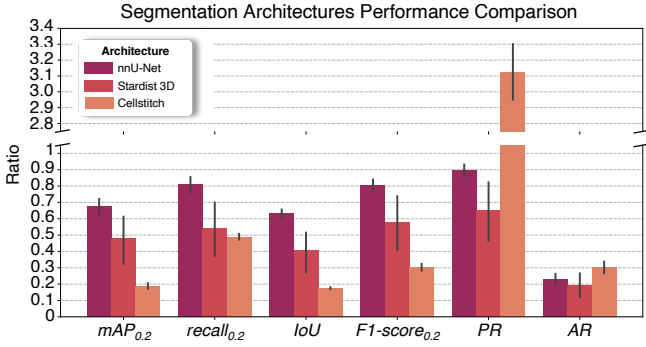
Cellstitch, a model based on Cellpose 2D, similarly to

Figure 1: Comparison of nnU-Net, Stardist 3D and Cellstitch.

the experiments in the 2D setting, also demonstrated the poorest performance in the 3D setting. Cellstitch largely over predicted the number of nuclei with a *PR* above 3 fold. On the other hand, Stardist 3D exhibited a tendency to underpredict the number of observations, resulting in inferior performance compared to nnU-Net.

Based on these observations, it can be concluded that training nnU-Net from scratch using the manually annotated dataset yields superior performance compared to open-source models. nnU-Net holds significant potential for further improvement, as enhancing the training dataset could elevate its performance even further, enabling a greater generalization capacity.

Notably, Stardist and Cellpose performance in 3D datasets is less extensively validated, with fewer studies and benchmarks compared to their well-documented effectiveness in 2D [16]. However, there should be considered the possibility that fine-tuning these models can improve their performance on the testing dataset. Likewise, their performance might achieve better results in different types of datasets as suggested in the literature [28, 29]. In fact, previous studies have reported that Stardist 3D can achieve a $mAP_{0.1}$ of 0.94, while Cellstitch reaches a $mAP_{\{0.3,0.5,0.7\}}$ of 0.66 – values that are considerably superior than those observed in our dataset. Specifically, when tested on dataset 1, Stardist 3D obtained a $mAP_{0.2}$ of 0.48 and Cellstitch a $mAP_{0.2}$ of 0.19, while nnU-Net obtained a value of 0.67.

4.4. Optimized nnU-Net model achieves outstanding prediction ratios

Despite nnU-Net had achieved better performance than Stardist 3D and Cellstitch, the prediction results were still suboptimal. This way nnU-Net models were further optimized in order to attain better performance os the testing dataset as well as greater generability. In particular, nnU-Net was trained on the five different datasets depicted on Table 2. These datasets tested the model's performance with different channel selection, augmentation strategies and FOV.

The results shown in Figure 2 indicate that preprocessing the data improved both the IoU score and the *AR* value when comparing *model 1* and *model 2*. These findings suggest that cleaner data with reduced noise enhances the recognition of nuclei borders, leading to sharper segmentations and less aggregation in predic-

tions. However, in an ideal scenario, preprocessing would not be necessary, as the model should be sufficiently robust to accurately segment individual instances without relying on additional data preparation.

Interestingly, when the network was trained using only the DAPI channel (*model 3*) instead of both the DAPI and GFAP channels (*model 2*), there was an improvement in both the IoU score and the *AR* value. This indicates that the GFAP channel hinders nuclei separation. Nevertheless, the GFAP channel positively impacted other metrics, implying that it may still play a role in aiding the model to identify nuclei positions. Overall, the results suggest that the GFAP channel is not desirable for nuclei segmentation tasks. Since it does not provide unequivocal benefits for nuclei segmentation and restricts the model's performance when applied to other datasets, training the model solely on the DAPI channel is a better approach.

The data augmentation strategies applied to datasets 4 and 5 were crucial in enhancing model performance without the GFAP channel. The performance of *model 4* and *model 5* was generally comparable; however, *model 5* was preferred due to its training on a more diverse and generalizable dataset, which incorporated image amplification as part of the data augmentation strategy. The zooming augmentation in dataset 5 enabled *model 5* to better adapt to images with varying FOV, making it particularly effective for evaluating unseen datasets.

Using a ranking-based scoring system, both *model 4* and *model 5* emerged as the top-performing models. However, due to the broader FOV range, *model 5* it is theoretically considered the most generalizable of the two.

4.5. nnU-Net model generalized successfully to hydrogel cultures datasets

The top-performing nnU-Net models, *model 4* and *model 5*, were tested on z-stacks of hydrogel astrocyte cultures and murine tissue samples. This experiment aimed to evaluate whether the models were generalizable to predict nuclei instances across different types of biological images.

Model 4 failed to predict nuclei instances in all tested images. While it performed effectively on the training dataset, this performance could not be generalized to datasets with varying FOV. Consequently, despite its success during validation, *model 4* is unsuitable for general-purpose applications.
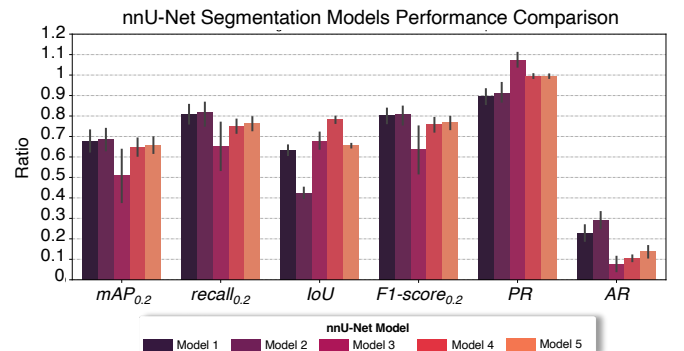

Figure 2: Comparison of nnU-Net optimization models.

In contrast, *model 5* yielded superior results, as demonstrated in Figure 3. It attained exceptional *PR* values across hydrogel cultures with single-cell organization, even across different FOV ranges. However, for tissue samples with densely packed cells, its performance was significantly inferior. These results indicate that while *model 5* does not produce robust predictions in a diverse array of image types, it performs exceptionally for nuclei segmentation in hydrogel cultures. These results underscore *model 5* utility for detecting cell nuclei in the cultures developed during this project.

The unseen datasets were evaluated based solely on the percentage of detected cells compared to the ground truth. Metrics such as the IoU and *AR* remain unassessed, as these evaluations require the unseen datasets to be annotated for nuclei segmentation. This lack of annotations is a bottleneck for further evaluation and was beyond the scope of this project.
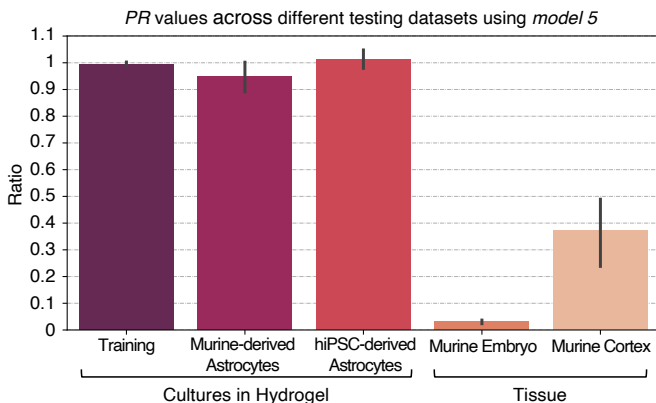

Figure 3: *PR* values across the different testing datasets using model 5 as predictor.

4.6. GUI for 3D cell culture image annotation with automatic identification of nuclei

A GUI was developed to address common challenges in biological image annotation, streamlining the process and enabling the creation of datasets for deep learning applications. This tool provides an intuitive and user-friendly platform for annotating large, multidimensional imaging datasets while overcoming limitations of existing software such as Fiji, particularly in terms of automation, usability, and data handling.

The GUI supports the annotation of 4D images (z-stacks with multiple color channels) and integrates data from a preprocessed .csv file generated by the nnU-Net model obtained in this project. This file contains detailed information about nuclei positions and bounding box dimensions, allowing users to load the data directly into the GUI for visualization and manual refinement. Detected nuclei are displayed as bounding boxes overlaying the image, with the option to correct missed or misclassified instances. By blending automated and manual steps, the tool ensures accuracy and efficiency in data annotation.

Two main types of classification are supported: morphological classification, tailored to specific experimental needs, and marker expression classification, which applies a more general binary scheme (Figure 4). Morphological categories are project-specific (i.e., round, branched, hBranched, cluster, other or unknown – see Subsection 2.8), reflecting the diverse phenotypes of astrocyte cultures in 3D hydrogels. Marker expression classification determines whether specific markers are present or absent in a cell, using a threshold-based semi-automatic approach. Predictions for marker presence are overly simplistic. The threshold-based method, which relies on the mean intensity within a bounding box, yields values exceeding eight times the mean intensity across the entire channel. This approach provides preliminary classifications that can be refined by the user.
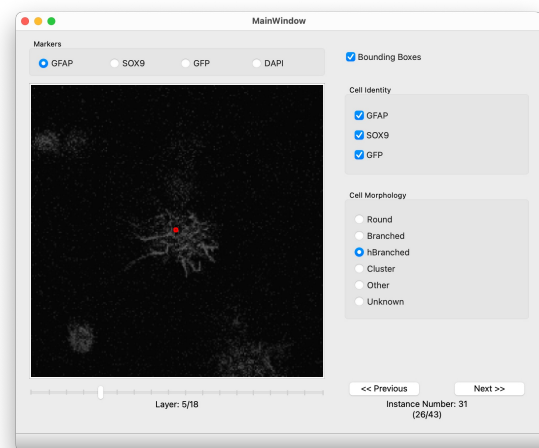

Figure 4: Representation of the GUI's Bounding Boxes window. Cell instance with 4 color channels: DAPI, GFP, SOX9, and GFAP, and 18 images depth. Instance number corresponds to the total number of instances identifies in the original image.

The GUI interface is designed to be both functional and accessible, offering tools for easy navigation through image stacks and color channels. Features such as shortcuts and optimized workflows significantly improve efficiency when annotating large datasets. The interface includes dedicated screens for bounding box inspection, enabling users to focus on individual nuclei instances, explore their depth and color information, and make detailed annotations. Additionally, the GUI allows sequential annotation of multiple images without interruption, automatically saving results in the original .csv file to prevent data loss and simplify subsequent data processing.

Unlike Fiji and similar tools, the GUI eliminates the need for manual copying, external spreadsheet handling, or repetitive re-navigation through datasets. Instead, it provides a streamlined environment for high-throughput annotation, empowering researchers to generate reliable datasets with minimal effort. Developed in Python using the PyQt5 library, the GUI has the potential to be adaptable to a range of experimental needs. It is currently shared with Helmholtz Munich collaborators via GitHub, with a user guide available for reference. By integrating semi-automation with user-friendly design, this tool represents a significant step towards making biological image annotation more efficient, scalable, and accessible for modern laboratory workflows.

5. Experimental Results and Discussion

5.1. FibrinVLVG hydrogels prove to be stable and exhibit astrocytes with in vivo-like morphologies

To evaluate astrocyte behavior in 3D hydrogel environments, three hydrogel types – MVG, VLVG, and FibrinVLVG – were tested with astrocytes derived from cortical GM of p5-7 Actin::GFP transgenic mice cultured for 7 days in vitro (DIV). The experimental workflow included the selective expansion of astrocytes, embedding in 15 μL hydrogel volumes within mini-wells, and analysis via immunostaining and confocal imaging after 7 DIV. Stability and cell morphology were evaluated qualitatively and quantitatively, with monolayer PDL-coated controls providing a baseline.

Key qualitative differences emerged during hydrogel casting and culture. MVG and VLVG hydrogels showed low stability and high heterogeneity. In addition, VLVG hydrogels presented substantial cell sedimentation, leading to decreased 3D cell density. Cells in MVG remained predominantly round due to restricted branching, while VLVG permitted some complexity but suffered significant degradation upon fixation. The limitations of MVG and VLVG hydrogels for cell culturing prevented thorough quantitative assessment of these conditions. In contrast, FibrinVLVG hydrogels demonstrated higher stability, limited degradation, and supported complex astrocytic morphologies resembling those found in vivo, characterized by distinct branching.

Through a morphological analysis, cells were categorized into six classes (Figure 5A). FibrinVLVG hydrogels exhibited fewer clusters in comparison to VLVG hydrogels – 6% against 22% of observed cells were in cell clusters – and more branched cells – 53% in FibrinVLVG against 38% in VLVG of the cells presented a branched or hBranched morphology (Figure 5B). However, the differences were not statistically significant due to variability and few biological replicates. SOX9 staining revealed astrocyte proportions exceeding 70% in all hydrogels. Hydrogel conditions showed higher reactive profiles among the astrocyte population, $GFAP^+/SOX9^+$ ratios, than the PDL control, although the difference is still not statistically significant.

FibrinVLVG hydrogels demonstrated superior stability and increased support for astrocytic morphology, positioning them as a promising 3D culture system for studying astrocyte cultures. These findings encouraged further characterization of FibrinVLVG hydrogels.

5.2. Different CaCl$_2$ concentrations does not impact cell viability on FibrinVLVG hydrogels

The effect of different CaCl$_2$ concentrations on cell viability in fibrin and FibrinVLVG hydrogels was studied over a 24-hour period. Cells were isolated from p5-7 mice, cultured for 7 days in astrocyte-selective media, and seeded into hydrogels at a density of 1.000.000 cells/mL. Hydrogel droplets (50 μL) were cast onto glass-bottom well plates, while a monolayer control was prepared on PDL-coated coverslips. Cell viability was evaluated using Hoechst 33342 to label all nuclei, calcein for live cells, and PI for dead cells. Five biological replicates were imaged using a STELLARIS 8 FALCON confocal microscope.

Cell viability classification revealed three populations: live (PI^-), dying ($Calcein^+PI^+$), and dead ($Calcein^-PI^+$) cells. Interestingly, some cells labeled with both calcein and PI, indicating dying phase (Figure 5C). These cells likely remained viable at the assay's start but lost membrane integrity during the incubation. Additionally, a subset of Hoechst-stained cells lacked both calcein and PI signals, hypothesized to be viable with unknown mechanisms preventing calcein uptake. Staining reagents appeared to diffuse evenly throughout the hydrogel, eliminating diffusion limitations as a variable.

Analysis of hydrogel cultures showed a higher proportion of dead and dying cells compared to monolayer controls (Figure 5D). In fibrin hydrogels, 87.64% of cells were viable, while FibrinVLVG hydrogels exhibited an average viability of 81.43% ± 2.12%. No significant difference in viability was observed between fibrin and FibrinVLVG conditions (p = 0.176). However, the 3D hydrogel environment significantly increased cell stress and death compared to monolayer cultures (p = 1.4×10^{-4}), suggesting that the matrix environment contributes to increased cellular stress.

The effect of CaCl$_2$ concentration on cell viability was analyzed using Pearson, r, and Spearman, ρ, correlation tests. No significant correlations were found between calcium levels and the proportion of live or dead cells. Pearson correlation yielded $r = 0.03$ (p = 0.93) for live cells and $r = 0.09$ (p = 0.78) for dead cells, while Spearman correlation showed $\rho = 0.15$ (p = 0.64) and $\rho = -0.065$ (p = 0.84), respectively. These findings imply that the calcium concentration within the tested range does not significantly influence cell viability in fibrin-based hydrogels.

5.3. Different CaCl$_2$ concentrations impact cell morphology and astrocytic marker expression on FibrinVLVG hydrogels

The influence of varying Ca^{2+} concentrations during hydrogel gelling is hypothesized to change hydrogel properties. Here there was studied how different crosslinking concentrations affect morphology and astrocytic marker expression on long-term 7 day cultures. Glial cells isolated from p5-7 WT mice were cultured in astrocyte-selective media for 7 days, embedded in hydrogels of different compositions and Ca^{2+} concentrations, and cultured during 7 days. Morphology and astrocytic marker expression analyses were performed using GFAP and SOX9 immunostaining.

Fibrin and 5 mM FibrinVLVG hydrogels exhibited rapid hydrogel degradation, compromising cell morphology and limiting data collection. Degradation occurred within 1–2 days for 5 mM FibrinVLVG and 6–7 days for fibrin hydrogels. Concentration of the Ca^{2+} solution used for gelling of FibrinVLVG hydrogels above 50 mM improved their stability. These stable conditions allowed for robust data collection and the observation of cellular responses.
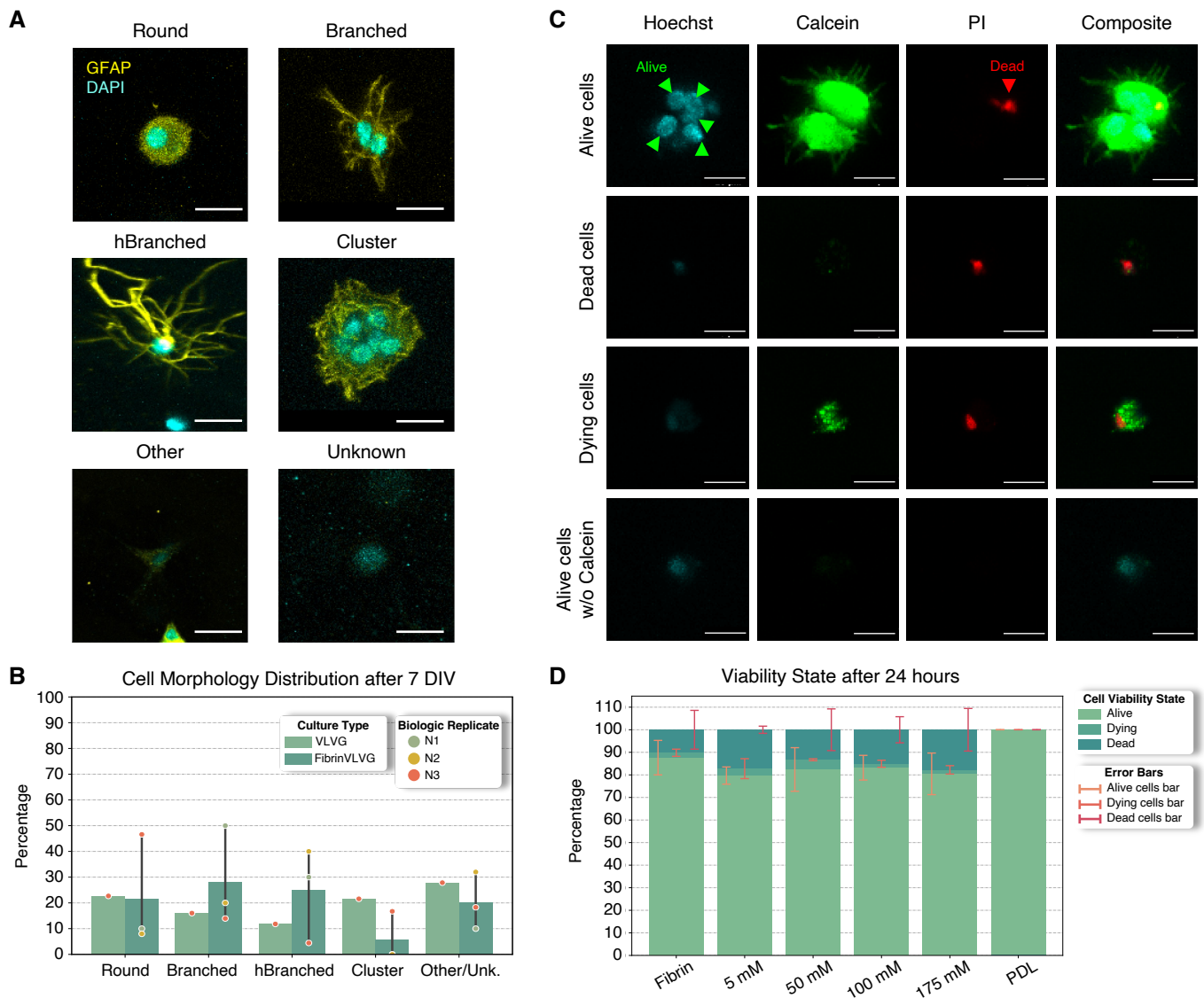
Figure 5: Categorization of cells regarding morphology and viability state. **(A)** Categorization of cells into round, branched, hBranched, cluster, other, and unknown classes. Scale bar = 15μm. **(B)** Cell morphology distribution in VLVG (N = 1) and FibrinVLVG hydrogels after 7 DIV (N = 3). **(C)** Categorization of cells regarding expression of viability markers. Scale bar = 20μm. **(D)** Viability essay analysis on VLVG and FibrinVLVG hydrogels crosslinked with 5 mM, 50 mM, 100 mM, and 175 mM of Ca^{2+}, comparing to monolayer cell cultures of PDL coated coverslips. The error bars indicate the standard deviation for each viability state, centered on the corresponding mean.

Morphological analysis revealed that increased Ca^{2+} concentrations were positively correlated with astrocytic branching (r = 0.32, p = 0.12), suggesting that higher stiffness promotes cellular ramification. Among tested conditions, 100 mM FibrinVLVG hydrogels supported the highest branching rates, with a percentage of 84.24%, while 5 mM FibrinVLVG exhibited the lowest, with merely 69.45% of the cells being ramified. Despite variability, most cells retained a branched morphology across all conditions (Figure 6A).

Cell identity analysis demonstrated that the stable hydrogel conditions – FibrinVLVG hydrogels gelled with at least 50 mM $CaCl_2$ concentration – consistently promoted a higher proportion of astrocytes, with an average above 85%, compared to monolayer controls, where average astrocytic ratio rounded 80%. Statistical analysis confirmed that hydrogel conditions significantly favored astrocyte selection over monolayer cultures (p = 0.04). More-

over, higher Ca^{2+} concentrations inversely correlated with GFAP expression, indicating a possible decrease in astrocytic reactivity (r = -0.60, p = 0.019). Similar trends observed for the $GFAP^+/SOX9^+$ ratio (r = -0.59, p = 0.020).

Correlations between morphology and marker expression highlighted that branched astrocytes showed higher GFAP expression than round cells (ρ = 0.35), suggesting a functional relationship between morphology and reactivity. As foreseen, cells classified as "Other" or "Unknown" were negatively correlated with both SOX9 and GFAP expression, reflecting non-astrocytic identities or absence of marker expression.

These findings emphasize the critical role of Ca^{2+} concentrations in shaping hydrogel properties, influencing astrocyte morphology, reactivity, and identity. Optimizing these parameters enhances the utility of hydrogels as 3D culture systems for astrocytic research and potentially other neural applications.
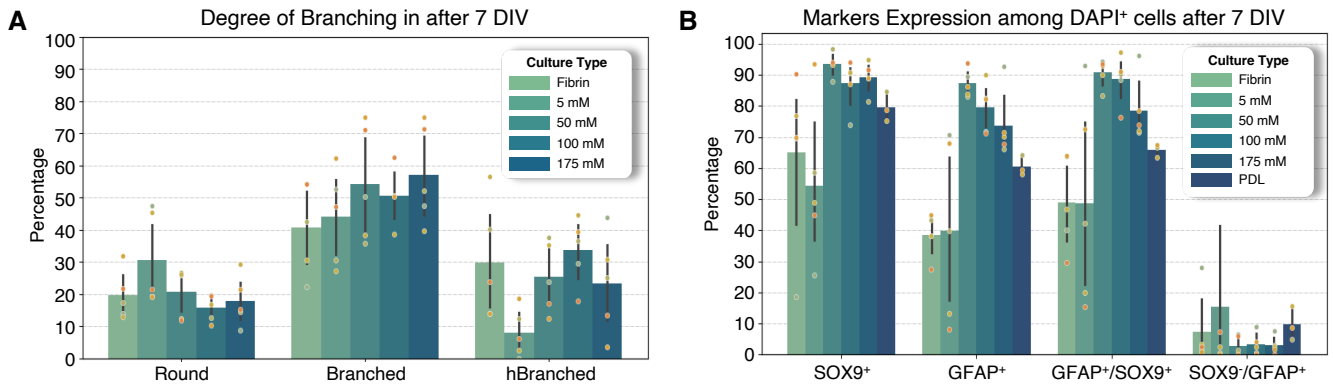
Figure 6: (A) Cell morphology analysis in Fibrin and FibrinVLVG hydrogels (N = 5). **(B)** astrocytic marker expression analysis on Fibrin and FibrinVLVG hydrogels crosslinked with 5 mM, 50 mM, 100 mM, and 175 mM of Ca^{2+}, comparing to monolayer cell cultures of PDL coated coverslips.

6. Conclusions

This project achieved meaningful contributions to the field of automated characterization of 3D astrocyte cultures in hydrogel matrices, leveraging a dual approach that integrates experimental and computational advancements. By addressing key challenges in both domains, this work provides a solid foundation for the optimization of 3D cell culture systems and their analysis, with implications for neurobiology and regenerative medicine.

In particular, advances were proposed along in three main fronts. Firstly, from the experimental validation of hydrogel systems stand point, the study provides a comprehensive evaluation of astrocyte morphology, viability, and marker expression in various hydrogel systems, identifying optimal conditions for future applications. Multiple hydrogel platforms, including MVG and VLVG alginate, fibrin, and their composite, FibrinVLVG, for astrocyte culturing were explored and validated. The results demonstrated that FibrinVLVG hydrogels, particularly those crosslinked with calcium chloride at 100 mM concentration, provided the most supportive microenvironment for murine astrocytes. These conditions promoted favorable cell viability, while also preserving key morphological features and the expression of astrocytic markers such as GFAP and SOX9. Comparative analysis revealed that 3D culture systems promote astrocyte reactive profiles when compared to monolayer systems, highlighting their potential for studying astrocyte behavior and heterogeneity under physiologically relevant conditions. However, cell death is also superior on these systems appealing further refinement of the methods.

Secondly, from the computational solutions perspective, this work takes an initial step towards the development of a high-throughput analysis pipeline for the characterization of astrocyte cultures, with special emphasis on nuclei segmentation and cell classification in 3D images. Using deep learning methods, the study compared the performance of different models, with nnU-Net emerging as a robust solution for accurate nuclei segmentation across multiple z-stack fluorescent microscopy images datasets. Furthermore, the integration of this tool into a user-friendly GUI streamlined the annotation and

analysis process, enabling researchers to efficiently label cell features and extract classification datasets. This automated approach reduces the time and expertise required for manual image analysis, paving the way for broader adoption in biological research.

Finally, considering the synergy between biology and computer science, this project takes a significant step towards bridging the gap between biological modeling and data-driven analysis, fostering more robust investigations into astrocyte biology. Automating image analysis has become indispensable in modern laboratories, as it not only accelerates workflows but also enhances the standardization and scalability of data processing. Consequently, the automation of these processes adds substantial value to research endeavors, enabling the generation and analysis of large, high-quality datasets with improved consistency and reliability.

The findings are promising, but several limitations, both experimental and computational, must be addressed in future endeavours. The project focused on a specific case study of culturing postnatal murine-derived astrocytes in alginate- and fibrin-based hydrogels. Ensuring the scalability of these experiments is crucial for broader applications. A better understanding of the interactions between fibrin-alginate hydrogels and astrocyte cultures is needed, as well as phenotypic studies using astrocytes from different sources. Further assessment of the physical and chemical properties of the hydrogels, including variations in crosslinking concentrations, is essential for a more holistic analysis.

From a computational standpoint, training deep learning models remains challenging due to the limited availability of annotated data. Exploring techniques for automating data annotation could improve model generalizability and streamline nuclei annotation. Additionally, using a nuclei detection model instead of segmentation model could reduce computational demands. Lastly, the GUI developed is currently specialized on hydrogel cell cultures. Extending these efforts for more general applications would leverage their outreach within the scientific community.

Acknowledgements

References

[1] Brent A Reynolds and Samuel Weiss. Generation of neurons and astrocytes from isolated cells of the adult mammalian central nervous system. *science*, 255(5052):1707–1710, 1992.

[2] Maria B Luskin. Restricted proliferation and migration of postnatally generated neurons derived from the forebrain subventricular zone. *Neuron*, 11(1):173–189, 1993.

[3] HA Cameron, CS Woolley, BS McEwen, and Elizabeth Gould. Differentiation of newly born neurons and glia in the dentate gyrus of the adult rat. *Neuroscience*, 56(2):337–344, 1993.

[4] Ashutosh Kumar, Vikas Pareek, Muneeb A Faiq, Sanjib K Ghosh, and Chiman Kumari. Adult neurogenesis in humans: a review of basic concepts, history, current research, and clinical implications. *Innovations in clinical neuroscience*, 16(5-6):30, 2019.

[5] Eric R Kandel, James H Schwartz, Thomas M Jessell, Steven Siegelbaum, A James Hudspeth, Sarah Mack, et al. *Principles of neural science*, volume 4. McGraw-hill New York, 2000.

[6] Md Mominur Rahman, Md Rezaul Islam, Md Yamin, Md Mohaimenul Islam, Md Taslim Sarker, Atkia Farzana Khan Meem, Aklima Akter, Talha Bin Emran, Simona Cavalu, and Rohit Sharma. Emerging role of neuron-glia in neurological disorders: at a glance. *Oxidative medicine and cellular longevity*, 2022(1):3201644, 2022.

[7] Tasuku Araki, Yuji Ikegaya, and Ryuta Koyama. The effects of microglia-and astrocyte-derived factors on neurogenesis in health and disease. *European Journal of Neuroscience*, 54(5):5880–5901, 2021.

[8] Annalisa Buffo, Milan R Vosko, Dilek Ertürk, Gerhard F Hamann, Mathias Jucker, David Rowitch, and Magdalena Götz. Expression pattern of the transcription factor olig2 in response to brain injuries: implications for neuronal repair. *Proceedings of the National Academy of Sciences*, 102(50):18183–18188, 2005.

[9] Magdalena Götz and Riccardo Bocchi. Neuronal replacement: Concepts, achievements, and call for caution. *Current opinion in neurobiology*, 69:185–192, 2021.

[10] Tetsuji Mori, Annalisa Buffo, and Magdalena Götz. The novel roles of glial cells revisited: the contribution of radial glia and astrocytes to neurogenesis. *Current topics in developmental biology*, 69:67–99, 2005.

[11] Julia C Fontoura, Christian Viezzer, Fabiana G Dos Santos, Rosane A Ligabue, Ricardo Weinlich, Renato D Puga, Dyeison Antonow, Patricia Severino, and Cristina Bonorino. Comparison of 2d and 3d cell culture models for cell growth, gene expression and drug resistance. *Materials Science and Engineering: C*, 107:110264, 2020.

[12] Lara S Costard, Ryan R Hosn, Harumi Ramanayake, Fergal J O'Brien, and Caroline M Curtin. Influences of the 3d microenvironment on cancer cell behaviour and treatment responsiveness: A recent update on lung, breast and prostate cancer models. *Acta Biomaterialia*, 132:360–378, 2021.

[13] Matthias P Lutolf and JA Hubbell. Synthetic biomaterials as instructive extracellular microenvironments for morphogenesis in tissue engineering. *Nature biotechnology*, 23(1):47–55, 2005.

[14] Hikmet Geckil, Feng Xu, Xiaohui Zhang, SangJun Moon, and Utkan Demirci. Engineering hydrogels as extracellular matrix mimics. *Nanomedicine*, 5(3):469–484, 2010.

[15] Ujith SK Madduma-Bandarage and Sundararajan V Madihally. Synthetic hydrogels: Synthesis, novel trends, and applications. *Journal of Applied Polymer Science*, 138(19):50376, 2021.

[16] Giona Kleinberg, Sophia Wang, Ester Comellas, James R Monaghan, and Sandra J Shefelbine. Usability of deep learning pipelines for 3d nuclei identification with stardist and cellpose. *Cells & Development*, 172:203806, 2022.

[17] Zhongqian Liu, Shijie Mao, Yubin Hu, Feng Liu, and Xiaowei Shao. Hydrogel platform facilitating astrocytic differentiation through cell mechanosensing and yap-mediated transcription. *Materials Today Bio*, 22:100735, 2023.

[18] Kuen Yong Lee and David J Mooney. Alginate: properties and biomedical applications. *Progress in polymer science*, 37(1):106–126, 2012.

[19] Paul A Janmey, Jessamine P Winer, and John W Weisel. Fibrin gels and their clinical and bioengineering applications. *Journal of the Royal Society Interface*, 6(30):1–10, 2009.

[20] Charlotte E Vorwald, Tomas Gonzalez-Fernandez, Shreeya Joshee, Pawel Sikorski, and J Kent Leach. Tunable fibrin-alginate interpenetrating network hydrogels to support cell spreading and network formation. *Acta biomaterialia*, 108:142–152, 2020.

[21] Yan Gao, Teena Sharma, and Yan Cui. Addressing the challenge of biomedical data inequality: An artificial intelligence perspective. *Annual review of biomedical data science*, 6(1):153–171, 2023.

[22] Erik Meijering. A bird's-eye view of deep learning in bioimage analysis. *Computational and structural biotechnology journal*, 18:2312–2325, 2020.

[23] Prathamesh M Kulkarni, Emily Barton, Michalis Savelonas, Raghav Padmanabhan, Yanbin Lu, Kristen Trett, William Shain, J Leigh Leasure, and Badrinath Roysam. Quantitative 3-d analysis of gfap labeled astrocytes from fluorescence confocal images. *Journal of neuroscience methods*, 246:38–51, 2015.

[24] Kaiming He, Georgia Gkioxari, Piotr Dollár, and Ross Girshick. Mask r-cnn. In *Proceedings of the IEEE international conference on computer vision*, pages 2961–2969, 2017.

[25] Uwe Schmidt, Martin Weigert, Coleman Broaddus, and Gene Myers. Cell detection with star-convex polygons. In *Medical Image Computing and Computer Assisted Intervention–MICCAI 2018: 21st International Conference, Granada, Spain, September 16-20, 2018, Proceedings, Part II 11*, pages 265–273. Springer, 2018.

[26] Carsen Stringer, Tim Wang, Michalis Michaelos, and Marius Pachitariu. Cellpose: a generalist algorithm for cellular segmentation. *Nature methods*, 18(1):100–106, 2021.

[27] Fabian Isensee, Paul F Jaeger, Simon AA Kohl, Jens Petersen, and Klaus H Maier-Hein. nnu-net: a self-configuring method for deep learning-based biomedical image segmentation. *Nature methods*, 18(2):203–211, 2021.

[28] Martin Weigert, Uwe Schmidt, Robert Haase, Ko Sugawara, and Gene Myers. Star-convex polyhedra for 3d object detection and segmentation in microscopy. In *Proceedings of the IEEE/CVF winter conference on applications of computer vision*, pages 3666–3673, 2020.

[29] Yining Liu, Yinuo Jin, Elham Azizi, and Andrew J Blumberg. Cellstitch: 3d cellular anisotropic image segmentation via optimal transport. *BMC bioinformatics*, 24(1):480, 2023.

[30] Christophe Heinrich, Sergio Gascón, Giacomo Masserdotti, Alexandra Lepier, Rodrigo Sanchez, Tatiana Simon-Ebert, Timm Schroeder, Magdalena Götz, and Benedikt Berninger. Generation of subtype-specific neurons from postnatal astroglia of the mouse cerebral cortex. *Nature protocols*, 6(2):214–228, 2011.